Supplementary Information for: Optogenetic control of migration of contractile cells predicted by an active gel model

Oliver M. Drozdowski[1,2]**, Falko Ziebert**[1,2]**, and Ulrich S. Schwarz**[1,2,+]

[1]Institute for Theoretical Physics, Heidelberg University, Philosophenweg 19, 69120 Heidelberg, Germany
[2]BioQuant, Heidelberg University, Im Neuenheimer Feld 267, 69120 Heidelberg, Germany
[+]Corresponding author: schwarz@thphys.uni-heidelberg.de

Supplementary Note 1: Analytical formula for bifurcation points

The bifurcation points of steady state solutions of the nonlinear system [Eq. (8) in the main manuscript] from the trivial branches can be shown to be given by solutions of

$$2\left[\cosh(\Omega) - 1\right] - \frac{\mathscr{P}\hat{c}}{\mathscr{A}\mathscr{D}(\hat{c})}\Omega\sinh(\Omega) = 0, \tag{S1}$$

with $\Omega^2 = [\hat{L}_\pm^2\mathscr{A}\mathscr{D}(\hat{c}) - \mathscr{P}\hat{L}_\pm^2\hat{c}]/[\mathscr{L}^2\mathscr{A}\mathscr{D}(\hat{c})]$ and $\hat{c} = 1/\hat{L}_\pm$. This implicit formula, generalizing a criterion given in Recho et al.[1] to the nonlinear diffusion case, implies that the bifurcation structure stays similar to the linear case $\mathscr{D}(c) \equiv 1$. Figure S1 shows the relaxation dynamics of the model, determining the stability of the branches. The full bifurcation diagram can be obtained using the continuation method[2] and is shown in Fig. S2.

Supplementary Note 2: Diffusion of Tonks gas and comparison to Taylor expansions

We found that for $e_A = 0$ (no attraction, only excluded volume, i.e., the Tonks gas) the concentration peaks in the motile steady state are still limited, but bistability does not occur. Thus, accelerating diffusion at high concentrations, as commonly assumed[3,4], is not sufficient in this thermodynamically consistent model to achieve bistability. We also find that one needs to be careful using a truncated Taylor expansion as this may result in changes in the criticality of the bifurcation for certain (unphysical) parameters of the full excluded volume interaction, as we will now explain.

For the Tonks gas of hard spheres on a line the nonlinear diffusion coefficient is equivalent to the van der Waals diffusion coefficient without any attractive energy ($e_A = 0$), i.e., analogously to Eq. (6) in the main text,

$$\mathscr{D}^{\text{Tonks}}(c) = \left(1 + \frac{c}{c_\infty - c}\right)^2, \tag{S2}$$

where $c_\infty = 1/N_A b$ with hard sphere diameter b. This model, henceforth called the Tonks gas, has the second order Taylor approximation

$$\mathscr{D}^{\text{Taylor}}(c) = 1 + \frac{2c}{c_\infty} + \frac{3c^2}{c_\infty^2}. \tag{S3}$$

Note that the linear term in the van der Waals fluid with attractive energy is $(2/c_\infty - e_A)c$, which means that a diffusion coefficient with vanishing linear term, as suggested in Ref.[3], is equivalent to $e_A = 2/c_\infty$, which is still supercritical and thus falls within our framework. Consequently, neglecting a linear term means that attraction has implicitly been considered.

Figure S3 depicts the bifurcation diagrams for the Tonks gas model, its second order Taylor approximation, the quadratic model with $e_A = 2/c_\infty$ and consistent volume exclusion, its Taylor approximation, the latter suggested in Ref.[3], and the linear Taylor approximation of the Tonks gas for different saturation concentrations c_∞. Note that in the Taylor approximations we have no divergence at $c = c_\infty$ and thus can look at saturation concentrations below the steady state concentration $c_\infty < \hat{c} = 1/\hat{L}_+ \approx 1.1$. For the second order Taylor approximation of the Tonks model we find bistability only in this regime inconsistent with the thermodynamic volume exclusion interpretation, while including such volume exclusion does not yield bistability. For the truncated quadratic model bistability is generally also in this inconsistent region or very close to $c_\infty = 1/\hat{L}_+$, not in agreement with experiments. In the case of linear dependence of diffusion on the concentration we do not find any bistability for saturation concentrations as low as $c_\infty = 0.01$, corresponding to an unreasonably large linear contribution (cf. Fig. S3(e)).

Effectively, truncating the Taylor expansion means that we introduce higher order terms cancelling the higher order terms of volume exclusion. These terms are not consistent with volume exclusion in the chemical potential and should not be neglected as in the nonlinear regime large concentrations are observed[4]. Hence, volume exclusion through the chemical potential alone cannot account for bistability if no cancelling effects in higher order terms are considered.

Supplementary Note 3: Length dynamics governed by integrated active stress

To study the effect of optogenetic activation, we included optogenetic activation in the active stress in the equation for stress [Eq. (8) in the main manuscript], $-\mathscr{P}/L\,c \to -(\mathscr{P}+\mathscr{E}\Xi)/L\,c$, and introduced a global myosin recruitment with saturation concentration c_∞ and recruitment rate $\mathscr{R}$. The full system of equations, modified from Eq. (8) in the main manuscript, then reads

$$\frac{\mathscr{L}^2}{L^2}\,\partial_u^2\sigma - \sigma = -\frac{\mathscr{P}+\mathscr{E}\Xi}{L}\,\tilde{c}, \tag{S4a}$$

$$\partial_t\tilde{c} + \frac{1}{L}\partial_u\left[\left(\frac{1}{\mathscr{A}L}\partial_u\sigma + \hat{v}\right)\tilde{c}\right] = \frac{1}{L^2}\partial_u[\mathscr{D}(\tilde{c}/L)\partial_u\tilde{c}] + \frac{\mathscr{R}}{L}\Xi\,\tilde{c}\,(Lc_\infty - \tilde{c}), \tag{S4b}$$

To see that length and velocity dynamics are governed by the integrated active stress and hence the integrated optogenetic signals, the equation for stress, Eq. (S4a), is integrated. The steady state length including optogenetic activation is then given by

$$\hat{L}_{\mathrm{act}} = 1 + \int_0^1 s(u)\mathrm{d}u - \int_0^1 [\mathscr{P} + \mathscr{E}\,\Xi(u)]\,c(u)\mathrm{d}u, \tag{S5}$$

with the stress deviation field from the boundary condition $s(u) = \sigma(u) + (L-1)$. Note that we assumed the signal Ξ to only depend on the internal position u, i.e., the cell is in a non-motile steady state or the activation region is moved along with the cell. Similarly to Ref.[5], we find that the steady state length is dominated by the active stress term, i.e., the last integral of the concentration field c in Eq. (S5).

Using the Green's function for σ from Eq. (S4a), one can see that the velocity V only depends on the antisymmetric part of the integrated active stress $-(\mathscr{P}+\mathscr{E}\Xi)c$ with respect to the cell center, $u = 1/2$, weighted by an appropriate integration kernel from the homogeneous solution. Thus the velocity also depends on the integrated active stress.

Supplementary Note 4: Continuation with optogenetic activation

For a localized contractility perturbation we introduced a sharp continuous representation of the left-half box function

$$\Xi(u) = \frac{1}{2}\left(1 + \tanh\left(\frac{1/2 - u}{0.001}\right)\right). \tag{S6}$$

We then used continuation for $\mathscr{R} = 0$ to calculate the bifurcation diagram for different activation strengths $\mathscr{E}$ for the same parameters as in Fig. 3(a) in the main manuscript with $e_{\mathrm{A}} = 0.63$, see Fig. S4(a). For optogenetic activation the pitchfork bifurcation separates into two saddle-node bifurcations, where the loss of stability of the previously non-motile solution is marked by the movement of the saddle node-bifurcation beyond the value of Pe. In Fig. S4(b) we continue the non-motile solutions ($V = 0$) for different Pe in $\mathscr{E}$. The saddle-node bifurcation, where branch switching occurs, if activated beyond, marks the activation threshold for motility initiation for fixed Pe. The stability threshold, shown in Fig. 6 in the main manuscript, is determined as the loci of this bifurcation in the $(\mathscr{A}, \mathscr{E})$ plane for fixed $\mathscr{L}^2\mathscr{A} = 1.25/77$.

Supplementary Note 5: Discontinuous Galerkin weak form of BVP

For the discontinuous Galerkin (dG) weak form we consider the interval $\Omega = [0,1]$ to be split into n_{mesh} equally sized subintervals K. In the following we denote with $\partial K \equiv \partial K\backslash\partial\Omega$ the boundary of subinterval K without external boundary points. We consider a function space of discontinuous functions on the subintervals. For a (test-)function ω the notation $\langle\omega\rangle = (\omega^{(+)} + \omega^{(-)})/2$ denotes the average of the two values left and right of the discontinuity, $\omega^{(+)}$ and $\omega^{(-)}$, respectively, and $[\![\omega]\!] = \omega^{(+)} - \omega^{(-)}$ is the difference or jump at the discontinuity. For the advection we define the upwind flux

$$\phi(\hat{v}c, n) = (\hat{v}cn - |\hat{v}cn|)/2 = \begin{cases} 0 & \hat{v}cn \geq 0, \quad \text{flow in direction } n \\ \hat{v}cn & \hat{v}cn < 0, \quad \text{flow against direction } n \end{cases}, \tag{S7}$$

where $n \in \{+1, -1\}$. We use the Symmetric Weighted Interior Penalty (SWIP) Finite Elements scheme. For this let $D^{(+)}$ and $D^{(-)}$ be the left and right diffusion constants at an interior face. Note that both (solely) depend on the concentration in the two subintervals and are therefore not constants but will have to be determined alongside with c. We define weights $\eta^{(+)}$ and $\eta^{(-)}$ such that $\eta^{(+)} + \eta^{(-)} = 1$, in particular[6],

$$\eta^{(\pm)} = \frac{D^{(\mp)}}{D^{(+)} + D^{(-)}}. \tag{S8}$$

Note the sign switch between η and D. We define the weighted average at the interfaces as $\langle \omega \rangle_\eta = \eta^{(+)} \omega^{(+)} + \eta^{(-)} \omega^{(-)}$. We also have to introduce a diffusion-dependent penalty factor, which is taken as the harmonic mean

$$\gamma_D = \frac{2 D^{(+)} D^{(-)}}{D^{(+)} + D^{(-)}} \tag{S9}$$

on inner faces and as $\gamma_D = D^{(\cdot)}$ at outer faces, where $(\cdot)$ represents the only existing sign.

For the stress we introduce the auxiliary field $s = \sigma + (L - 1)$ for which we have homogeneous Dirichlet boundary conditions. The weak form of Eq. (S4a) reads

$$
\begin{aligned}
0 = \sum_K \Bigg\{ &\int_K \frac{\mathscr{L}^2}{L^2} (\partial_u s)(\partial_u \omega)\, \mathrm{d}V + \int_K \left[s - (L-1) - \frac{\mathscr{P} + \mathscr{E}\Xi}{L} c \right] \omega\, \mathrm{d}V \\
&+ \int_{\partial K} \frac{\mathscr{L}^2}{L^2} \frac{\alpha}{h} [\![sn]\!][\![\omega n]\!]\, \mathrm{d}S - \int_{\partial K} \frac{\mathscr{L}^2}{L^2} \langle \partial_u s \rangle [\![\omega n]\!]\, \mathrm{d}S - \int_{\partial K} \frac{\mathscr{L}^2}{L^2} \langle \partial_u \omega \rangle [\![sn]\!]\, \mathrm{d}S \Bigg\} \\
&+ \int_{\partial \Omega} \frac{\mathscr{L}^2}{L^2} \frac{\alpha}{h} s\, \omega\, \mathrm{d}S - \int_{\partial \Omega} \frac{\mathscr{L}^2}{L^2} (\partial_u s)\, \omega n\, \mathrm{d}S - \int_{\partial \Omega} \frac{\mathscr{L}^2}{L^2} s\, (\partial_u \omega) n\, \mathrm{d}S,
\end{aligned}
\tag{S10}
$$

where ω is an appropriate test function, h is the mesh size, n is the outward pointing normal $n = \pm 1$, and α is the Nitsche parameter, chosen to be $\alpha = 5$ in this work. The first line of Eq. (S10) is the weak form for a solution inside the subintervals. The second line implements consistency and symmetry, and penalizes jumps at interior interfaces. The third line is a weak version of the homogeneous Dirichlet boundary condition $s(0) = 0 = s(1)$.

For the concentration equation, Eq. (S4b), we introduce the full advection velocity $\hat{\beta} = \left(\frac{1}{\mathscr{A}L} \partial_u \sigma + \hat{v} \right)$ and obtain the weak form

$$
\begin{aligned}
0 = \sum_K \Bigg\{ &\int_K \frac{\tilde{c} - \tilde{c}^{(-1)}}{\Delta t}\, \mathrm{d}V - \int_K \frac{1}{L} \hat{\beta}^{(-1)} \tilde{c}\, (\partial_u \omega)\, \mathrm{d}V + \int_K \frac{1}{L^2} \mathscr{D}(\tilde{c}/L)(\partial_u \tilde{c})(\partial_u \omega)\, \mathrm{d}V - \int_K \frac{\mathscr{R}}{L} \Xi \tilde{c}\, (Lc_\infty - \tilde{c})\, \omega\, \mathrm{d}V \\
&+ \int_{\partial K} \frac{\gamma_D}{L^2} \frac{\alpha}{h} [\![\tilde{c}n]\!][\![\omega n]\!]\, \mathrm{d}S - \int_{\partial K} \frac{1}{L^2} \langle \mathscr{D}(\tilde{c}/L) \partial_u \tilde{c} \rangle_\eta [\![\omega n]\!]\, \mathrm{d}S - \int_{\partial K} \frac{1}{L^2} \langle \mathscr{D}(\tilde{c}/L)(\partial_u \omega) \rangle_\eta [\![\tilde{c}n]\!]\, \mathrm{d}S \\
&+ \int_{\partial K} \frac{1}{L} [\![\omega n]\!] \left(\phi(\hat{\beta}^{(-1)(+)} \tilde{c}^{(+)}, n) - \phi(\hat{\beta}^{(-1)(-)} \tilde{c}^{(-)}, n) \right)\, \mathrm{d}S \Bigg\},
\end{aligned}
\tag{S11}
$$

where the superscript (-1) denotes quantities from the previous timestep. We thus use an implicit Euler scheme but with the advection velocity $\hat{\beta}$ given by the solution of the stress equation in the last step. Note that the Neumann boundary condition $\partial_u \tilde{c}(u_\pm, t) = L \hat{\beta} \tilde{c}(u_\pm, t) / \mathscr{D}(\tilde{c}/L)$ from motor conservation is implicitly incorporated: the advection term drops out as we would need to introduce it with a different sign to enforce the advection flux at the boundary.

Supplementary References

1. Recho, P., Putelat, T. & Truskinovsky, L. Mechanics of motility initiation and motility arrest in crawling cells. *J. Mech. Phys. Solids* **84**, 469 – 505 (2015).

2. Doedel, E. J. *et al.* AUTO-07P: Continuation and bifurcation software for ordinary differential equations (2007).

3. Chelly, H. & Recho, P. Cell motility as an energy minimization process. *Phys. Rev. E* **105**, 064401 (2022).

4. Recho, P., Putelat, T. & Truskinovsky, L. Contraction-Driven Cell Motility. *Phys. Rev. Lett.* **111**, 108102 (2013).

5. Drozdowski, O. M., Ziebert, F. & Schwarz, U. S. Optogenetic control of intracellular flows and cell migration: A comprehensive mathematical analysis with a minimal active gel model. *Phys. Rev. E* **104**, 024406 (2021).

6. Ern, A., Stephansen, A. F. & Zunino, P. A discontinuous galerkin method with weighted averages for advection–diffusion equations with locally small and anisotropic diffusivity. *IMA J. Numer. Anal.* **29**, 235–256 (2009).

7. Verkhovsky, A. B., Svitkina, T. M. & Borisy, G. G. Self-polarization and directional motility of cytoplasm. *Curr. Biol.* **9**, 11 – S1 (1999).

8. Barnhart, E. L., Lee, K.-C., Keren, K., Mogilner, A. & Theriot, J. A. An adhesion-dependent switch between mechanisms that determine motile cell shape. *PLOS Biol.* **9**, 1–19 (2011).

9. Oakes, P. W. *et al.* Optogenetic control of RhoA reveals zyxin-mediated elasticity of stress fibres. *Nat. Commun.* **8**, 15817 (2017).

10. Uehara, R. *et al.* Determinants of myosin II cortical localization during cytokinesis. *Curr. Biol.* **20**, 1080–1085 (2010).

11. Luo, T. *et al.* Understanding the cooperative interaction between myosin II and actin cross-linkers mediated by actin filaments during mechanosensation. *Biophys. J.* **102**, 238–247 (2012).

12. Kolega, J. & Taylor, D. L. Gradients in the concentration and assembly of myosin II in living fibroblasts during locomotion and fiber transport. *Mol. Biol. Cell* **4**, 819–836 (1993).

13. Loosley, A. J. & Tang, J. X. Stick-slip motion and elastic coupling in crawling cells. *Phys. Rev. E* **86**, 031908 (2012).

14. Vallotton, P., Danuser, G., Bohnet, S., Meister, J.-J. & Verkhovsky, A. B. Tracking retrograde flow in keratocytes: News from the front. *Mol. Biol. Cell* **16**, 1223–1231 (2005).

quantity	used value	literature values
cell length L_0	$20\,\mu$m	$20\,\mu$m[7]
(bulk) viscosity η	$10^5\,$Pa	$10^5\,$Pa[8]
active stress χc_0	$10^2\,$Pa	$10^2\,$Pa[8] $330\,$Pa[9]
drag coefficient ξ	$2 \times 10^{14}\,$Pa s m^{-2}	$2 \times 10^{16}\,$Pa s m^{-2} (large adhesion)[8] $2 \times 10^{14}\,$Pa s m^{-2} (medium adhesion)[8] $4 \times 10^{13}\,$Pa s m^{-2} (low adhesion)[8]
myosin diffusion D	$0.7\,\mu$m^2 s^{-1}	$0.8\,\mu$m^2 s^{-1}[18,10] $0.2\,\mu$m^2 s^{-1}[11] $0.6 - 1.3\,\mu$m^2 s^{-1}[12]
cortex stiffness k	$10^3\,$Pa	$10^3 - 10^4\,$Pa[8,13]
polymerization velocity v_p	4% total speed	$1 - 3\,\mu$m min^{-1} (5 − 15% total speed)[14]
saturation concentration c_∞/c_0	10	$\gtrsim 4$ (20 − 40% length myosin-enriched)
attractive interaction e_{A}	0.63	−
Pe $= k/\xi D$	$70 - 90$ we use 77	
$\mathscr{L}^2 = \eta/(\xi L_0^2)$	1.25	
$\mathscr{P} = \chi c_0/k$	0.1	

Supplementary Table 1. Parameters used within this study to determine the dimensionless parameters Pe, $\mathscr{L}^2$, and $\mathscr{P}$ with the resulting values. Literature values for the parameters are given to give a possible range for the parameter choice.
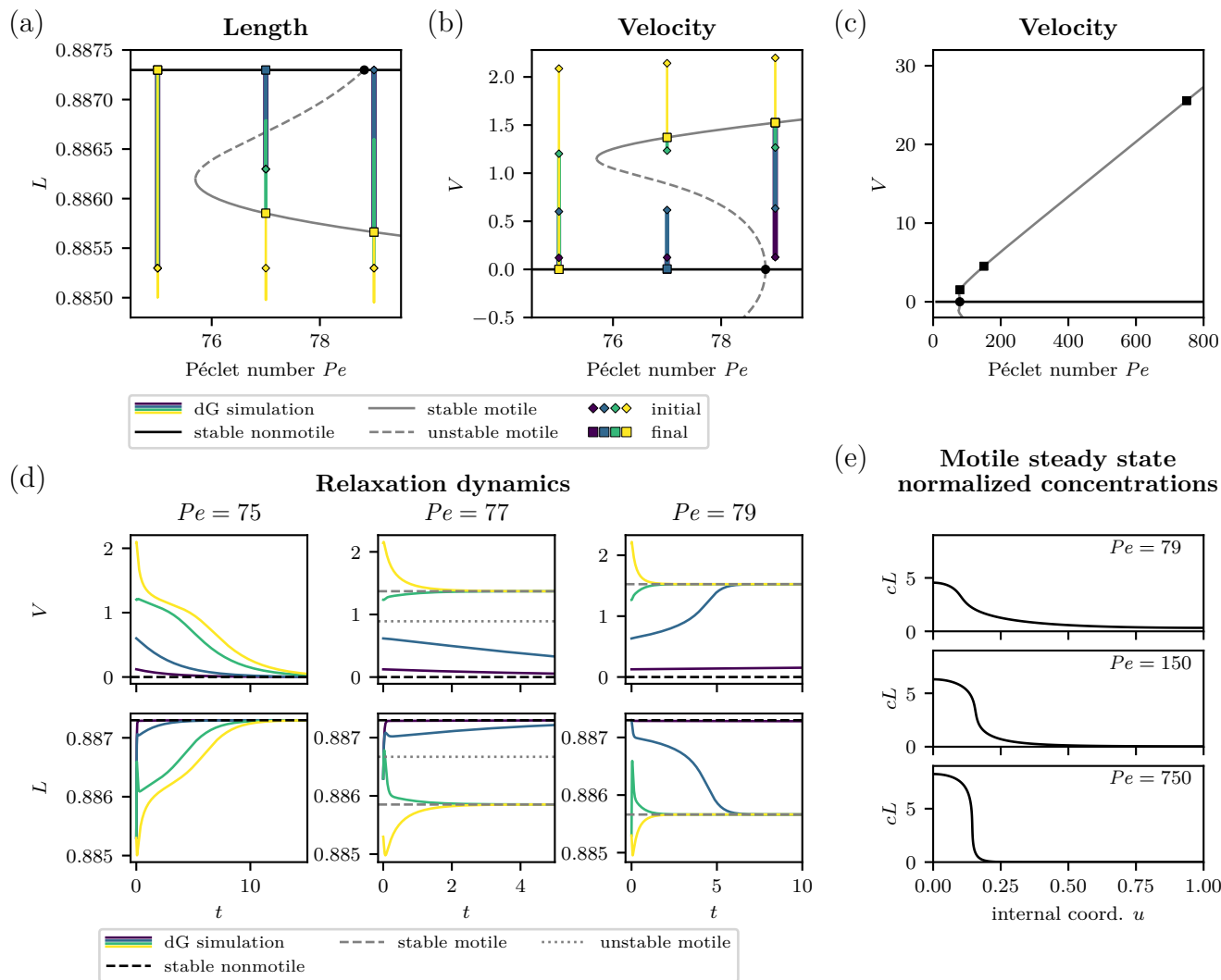
Supplementary Figure 1. Different initial states relax toward the stable steady states. Panel (a) shows the bifurcation diagram in length with the trajectories in parameter space of relaxation simulations, shown in Panel (d). Panels (b) and (c) show the bifurcation diagrams in velocity in the bistable region and a larger range, respectively. Panel (d) shows discontinuous Galerkin (dG) simulations of relaxation toward the stable steady states for different Péclet numbers Pe. Depicted are both the velocity V and length L as functions of simulation time t. Note that the relaxation of the length is nontrivial and crossings over multiple solution branches occur. Panel (e) depicts the normalized concentration profiles cL in internal coordinates u for different Pe. We observe that for large Pe a myosin-enriched layer develops in the concentration. The different parameters Pe are marked in the corresponding bifurcation diagram in Panel (c) as black squares. Parameters: $\mathscr{P} = 0.1$, $\mathscr{L}^2 = 1.25$, $e_A = 0.63$, $c_\infty = 10$.
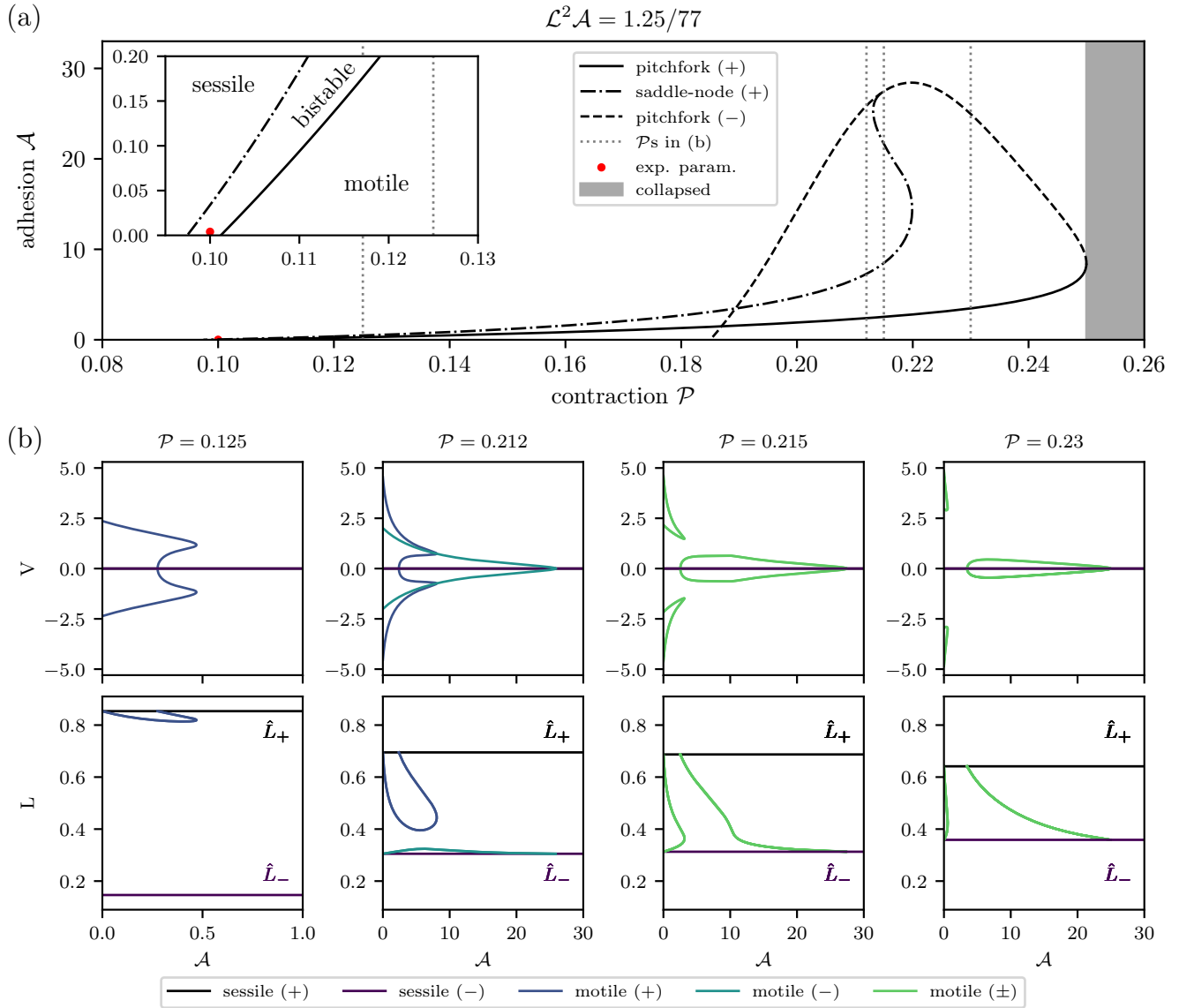
Supplementary Figure 2. Full diagram showing the loci of bifurcations. We consider $\mathcal{L}^2\mathcal{A} = 1.25/77$. For strong contraction $\mathcal{P} \geq 1/4$ we have collapse of the solution, as in the linear model. The loci of the pitchfork and saddle node bifurcations have been continued and are shown in Panel (a). Panel (b) depicts bifurcation diagrams of velocity V and length L in adhesion $\mathcal{A}$ for different contractilities $\mathcal{P}$, indicated as vertical lines in Panel (a). Increasing $\mathcal{P}$ from experimental parameters we first obtain a second motile solution bifurcating from the sessile $(-)$ branch, which we have neglected in the main text, as these solutions are not stable or do not exist in the experimentally relevant range. After that the motile branches $(+)$ and $(-)$ merge and we obtain two motile branches, connecting the two sessile $(+)$ and $(-)$ branches, denoted with $(\pm)$. Parameters: $e_A = 0.63$, $c_\infty = 10$.
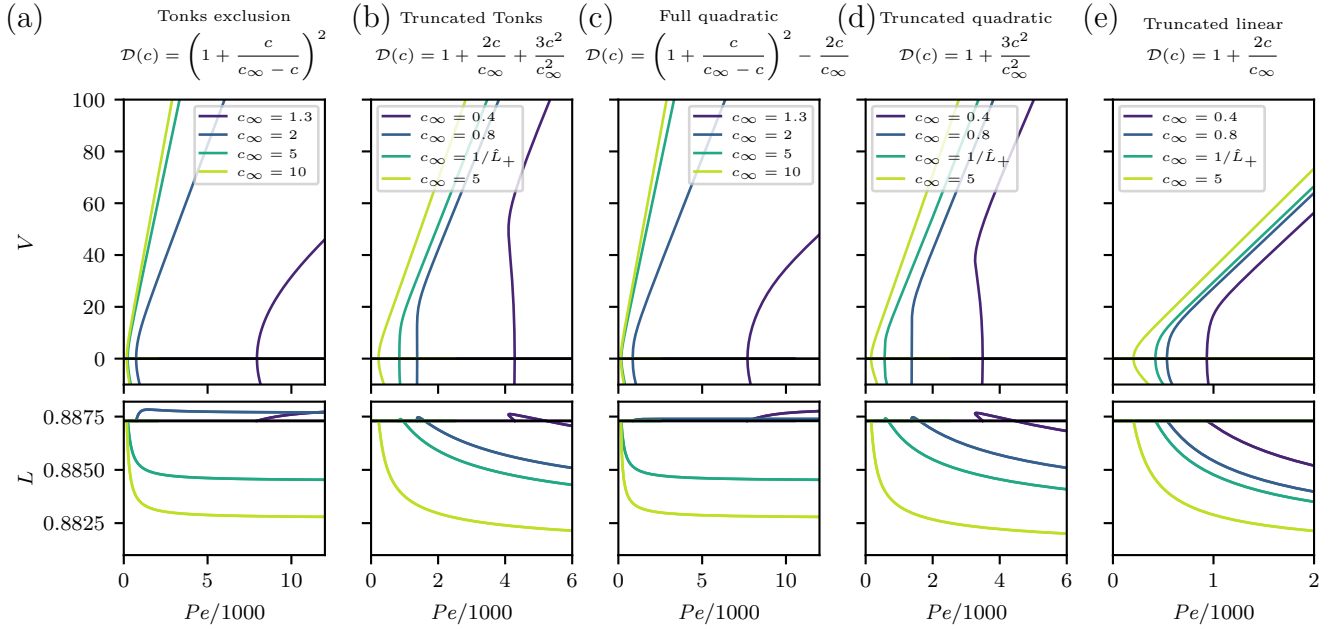
Supplementary Figure 3. Bifurcation diagrams for different nonlinear diffusion models. We show nondimensionalized velocity V and length L as functions of the Péclet number Pe for different models with volume exclusion. (a) Tonks gas model, which is the van der Waals model without attraction. (b) Second order Taylor approximation of the Tonks gas. (c) Full quadratic model, i.e., the van der Waals fluid with $e_A = 2/c_\infty$, such that the linear term cancels. (d) Second order Taylor approximation of the quadratic model. The term linear in concentration c vanishes. (e) Linear Taylor approximation of the Tonks gas. In the truncated models we find bistability only for quadratic diffusion in a regime inconsistent with the Tonks gas, see text. Parameters: $\mathscr{P} = 0.1$, $\mathscr{L}^2 = 1.25$
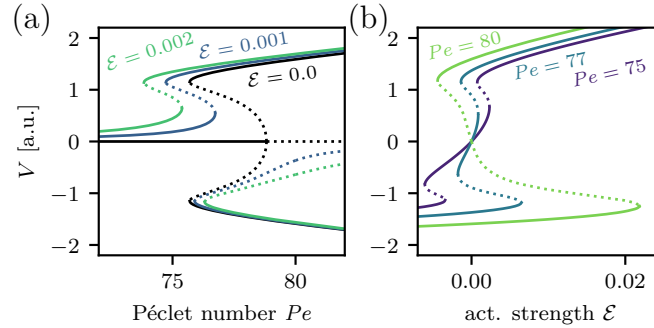
Supplementary Figure 4. Bifurcation diagram of the model with nonlinear diffusion for optogenetic activation in the left half. Velocities V of solution branches for continuation in the Péclet number Pe for different optogenetic activation strengths $\mathscr{E}$ (a) and for continuation in $\mathscr{E}$ for different Pe (b). (a) The pitchfork bifurcation separates into two saddle-node bifurcations for optogenetic activation with activation strength $\mathscr{E} > 0$, which move apart for increasing activation. (b) In the bistable regime we have coexistence of multiple solutions for small activation strengths $\mathscr{E}$. However, if the non-motile solution is stable without activation, increasing activation will lead to motility and the cell jumps to the motile solution branch if activation increases beyond the saddle-node bifurcation. Parameters like in Fig. 3(a) in the main manuscript, i.e., $\mathscr{L}^2 = 1.25$, $\mathscr{P} = 0.1$, $c_\infty = 10$, $e_A = 0.63$.
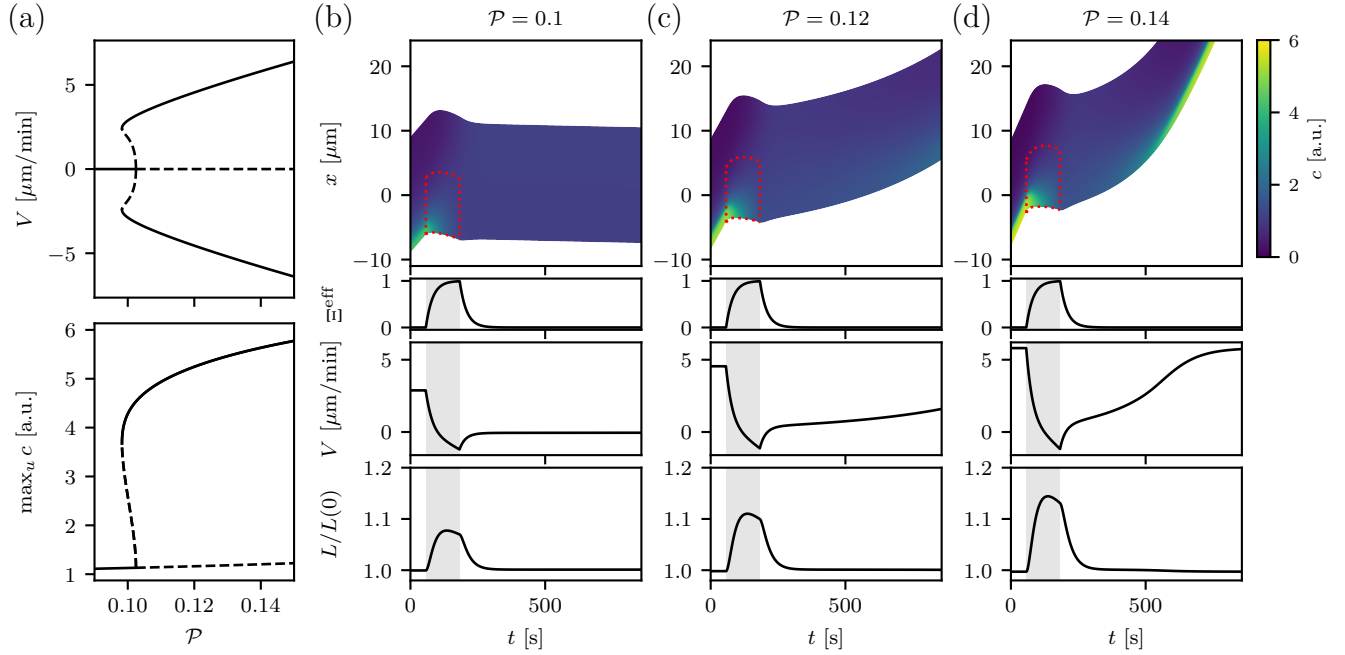
Supplementary Figure 5. Contractility determines relaxation behavior after optogenetic inhibition. Varying the dimensionless contractility $\mathscr{P}$ changes the outcome of simulations with inhibitory optogenetic perturbations. (a) Bifurcation diagrams in velocity V and maximal concentration polarization $\max_u c$ as functions of the control parameter contractility $\mathscr{P}$. For $\mathscr{P} = 0.1$, as used throughout the manuscript, bistability occurs. Increasing the total contractility leads to the loss of bistability, an increase in V in the stable motile state and a more strongly pronounced peak in the concentration field. (b-d) Kymographs of concentration in space as functions of time for different contractilities and temporal activation Ξ^{eff}, velocity V and relative length change $L/L(0)$. The optogenetic activation strength is $\mathscr{E} = -0.9\mathscr{P}$ for all simulations. Note that the relaxation toward the motile state occurs faster for larger $\mathscr{P}$, no motility arrest occurs for large $\mathscr{P}$, but the relative strength of the velocity perturbation is comparable. In particular, the velocity drops below 0 to similar values for all $\mathscr{P}$, suggesting that the relative activation strength $\mathscr{E}/\mathscr{P}$ and activation time determine the velocity change during activation. Other parameters chosen identical to Fig. 7(d).